Journal of Computational and Applied Mathematics 414 (2022) 114438

Contents lists available at ScienceDirect

Journal of Computational and Applied Mathematics

journal homepage: www.elsevier.com/locate/cam

Isogeometric analysis using a tensor product blending spline construction

Tatiana Kravetc

R&D group Simulations, Department of Computer Science and Computational Engineering, Faculty of Engineering Science and Technology, UiT – The Arctic University of Norway, Norway

ARTICLE INFO

Article history:
Received 18 September 2020
Received in revised form 6 April 2022

Keywords:
Isogeometric analysis
Blending splines
Expo-rational basis functions
hp-refinement

ABSTRACT

In this paper, we introduce a blending spline type construction into the isogeometric analysis. We consider a general algorithm for solving a number of boundary value problems, including heat equation, wave equation, linear elasticity, etc. The usage of blending spline construction in the isogeometric context mixes standard finite element and NURBS-based approaches while accumulating the benefits of both. Since the blending spline construction is locally represented, the finite element discretization can be formulated in a standard way, while the smooth representation of these splines provides an accurate approximation of the computational domain even on a coarse mesh.

Besides the standard L^2-projection algorithm for the domain approximation, we demonstrate a unique scheme for domain construction based on local surfaces and subsequent hp-refinement.

In the proposed paper we focus on the features of blending splines in the isogeometric analysis context, identify possible applications, and provide some numerical analysis.

1. Introduction

Isogeometric analysis (IGA) [1] is a generalization of the standard finite element method. The main idea of the isogeometric concept is that the same basis functions are used for both geometry description and analysis. In contrast to standard polynomial elements, which give a continuous but not smooth solution, the isogeometric representation is typically smooth. The usage of a smooth basis is efficient in many areas including structural analysis [2–4], fluid–structure interaction [5], phase-field models [6], etc. Currently, a standard tool for isogeometric analysis is the non-uniform B-splines (NURBS) [7,8] and their modifications, such as Hierarchical B-splines, T-splines, LR-splines. These modifications are successfully used for local refinement in the isogeometric analysis [9–12].

Refinement schemes are essential for improving the solution in both the standard finite element method and isogeometric analysis. Besides standard *h*-refinement and *p*-refinement, the isogeometric approach using a B-spline basis supports a combination of these two refinement schemes when both degree and mesh density are increased. In addition, increasing the spline degree leads to higher continuity of the function, which is one of the important features of NURBS-based isogeometric analysis.

Blending spline type construction is an alternative tool for geometric modeling and isogeometric analysis, firstly introduced in [13]. In contrast to B-splines, the support of blending spline basis functions does not depend on their degree, in other words, the locality of the basis is always maintained. Blending spline representation in application to

E-mail address: tatiana.kravetc@uit.no.

https://doi.org/10.1016/j.cam.2022.114438

isogeometric framework accumulates the benefits of both B-spline and standard finite element approaches. A concept of blending splines is founded on blending basis functions, in particular, expo-rational basis functions (ERBS) and their generalizations (GERBS) [14]. Some related work regarding the utilization of expo-rational B-splines in finite element context can be found in [15,16].

Blending spline construction has a hierarchical (multilayer) structure, i.e. parametric local geometries are blended by underlying basis function to form global surface patches. An ordered set of global surface patches forms a smooth global surface due to the overlapping of local surfaces. Local surfaces contain information about global surface derivatives at the knots. The independence of local surfaces from each other allows for flexible modeling and flexible inner parameterization of the global surface.

Spline spaces that are a tensor product of two univariate spline spaces are standard for surface representation in computer-aided design (CAD) and IGA. Blending splines naturally support tensor product surfaces that can be locally refined by knot insertion [17]. In addition, the blending splines allow for more flexible surface constructions, such as triangulated surfaces [18,19] and polygonal surfaces [20].

The novelty of this paper is to examine the utilization of blending spline construction in the isogeometric analysis framework. We present a new approach to the blending basis function evaluation such that it can be successfully applied to the finite element analysis context. In addition, we demonstrate a unique method for computational domain modeling technique using blending splines.

The proposed paper consists of the following sections. Section 2 describes an evaluation of the blending spline constructions and corresponding basis functions with a purpose for application in the analysis. Section 3 focuses on the methods for modeling 2D domains. In Section 4 we formulate the general procedure of applying the isogeometric approach to solving various boundary value problems. Section 5 provides several examples of the usage of blending spline construction for solving different physical problems. Finally, we summarize the proposed work and identify research questions for future development in Section 6.

2. Blending type spline construction

We now consider some of the theory of blending type spline constructions, which is relevant for this work. A detailed study of the expo-rational B-splines (ERBS) can be found in [13,21].

Let Φ be a one-dimensional domain with $u \in [0, 1]$ as a parameter subdivided into m_u intervals. An open knot vector defined on Φ has two multiple knots on both sides. The knots are numerated from 0 to $m_u + 2$. The simple version of an expo-rational basis function associated with the strictly increasing knots u_{k-1}, u_k and u_{k+1}, $k = 1, \ldots, m_u + 1$, is defined in [21] as

$$B_k(u) = \begin{cases} \Gamma_{k-1} \displaystyle\int_{u_{k-1}}^{u} \phi_{k-1}(s)ds, & u_{k-1} < u \leq u_k, \\ \Gamma_k \displaystyle\int_{u}^{u_{k+1}} \phi_k(s)ds, & u_k < u < u_{k+1}, \\ 0, & \text{otherwise}, \end{cases} \tag{1}$$

where

$$\phi_k(u) = \exp\left(-\frac{\left(u - \dfrac{u_k + u_{k+1}}{2}\right)^2}{(u - u_k)(u_{k+1} - u)} \right),$$

and the scaling factor

$$\Gamma_k = \frac{1}{\int_{u_k}^{u_{k+1}} \phi_k(u)du}.$$

Fig. 1(c) demonstrates the expo-rational basis function (1) with support on two neighbor knot intervals. In the blending construction, the expo-rational basis functions are used as functions that blend together overlapped local geometry. Fig. 1(a) shows a part of the domain Φ and identifies supports of the overlapped local curves ℓ_k, $k = 1, \ldots, m_u + 1$. In our particular case, we choose Bézier curves (Bézier surfaces for the two-dimensional case) as local geometry. Each Bézier curve is defined as a linear combination of control points and Bernstein polynomials. Moreover, they are scaled and translated to the interval $[u_{k-1}, u_{k+1}]$, as shown in Fig. 1(b). For this, we introduce a local/global mapping $\omega_k(u)$, which scales the support of the local curves ℓ_k to the interval $[u_{k-1}, u_{k+1}]$.

$$\omega_k(u) = \begin{cases} \dfrac{u - u_{k-1}}{u_{k+1} - u_{k-1}}, & u_{k-1} < u \leq u_{k+1}, \\ 0, & \text{otherwise}. \end{cases}$$

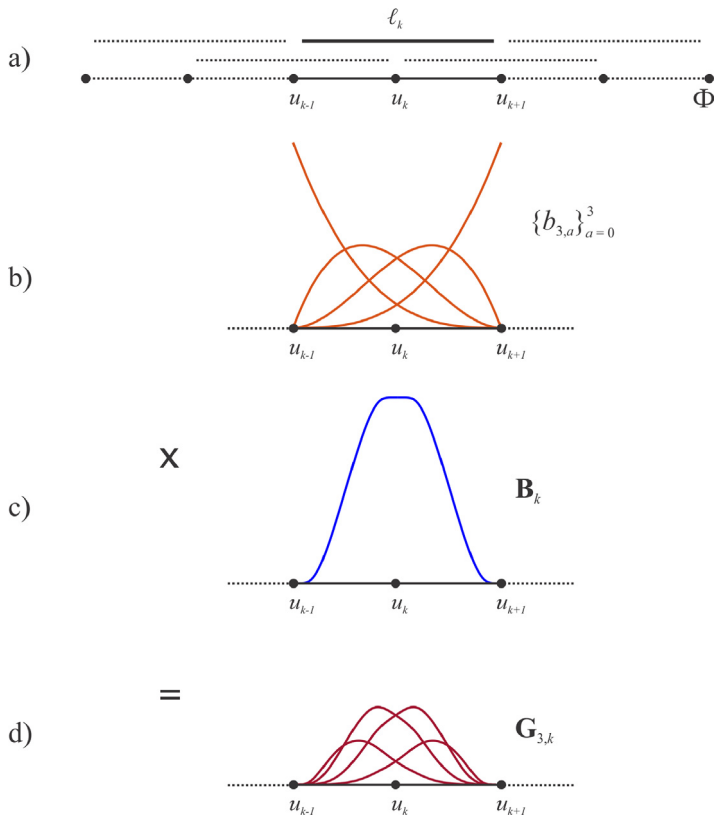

Fig. 1. The construction process of the univariate combined expo-rational basis $\mathbf{G}_{3,k}$ on example of kth node. (a) One-dimensional domain Φ, and kth node support covered with local curve ℓ_k. (b) A set of Bernstein polynomials $\{b_{3,a}\}_{a=0}^{3}$ forming a basis of the local curve ℓ_k. (c) Underlying expo-rational basis function $\mathbf{B}_k$. (d) A set of combined expo-rational basis functions $\mathbf{G}_{3,k}$ obtained by sequential multiplication of the expo-rational basis function and corresponding Bernstein polynomials.

Thus, the local Bézier curve ℓ_k, $k = 1, \ldots, m_u + 1$ is defined as

$$\ell_k = \sum_{a=0}^{d} b_{d,a}(\omega_k(u))\, q_{k,a}, \tag{2}$$

where $q_{k,a}$ are control points of the kth local curve, and $b_{d,a}$ are Bernstein polynomials of degree d, which are generated by the general formula

$$b_{d,a}(t) = \binom{d}{a} t^a (1-t)^{d-a} = \frac{d!}{a!(d-a)!}\, t^a (1-t)^{d-a}, \quad a = 0, \ldots, d.$$

Using (1) and (2), we describe the expo-rational B-spline curve as

$$A(u) = \sum_{k=1}^{m_u+1} B_k(u)\ell_k. \tag{3}$$

In order to apply the isogeometric method to the blending splines, we merge underlying expo-rational basis functions and local Bernstein polynomials as follows

$$\mathbf{G}_{d,k} = \{B_k\, b_{d,a}(\omega_k(u))\}_{a=0}^{d}. \tag{4}$$

The set of functions $\mathbf{G}_{d,k}$ (4) is called a set of combined expo-rational basis functions of local degree d evaluated under kth local curve. An example of evaluating the set $\mathbf{G}_{3,k}$ is shown in Fig. 1. Comparison of combined expo-rational basis functions and B-spline basis functions in the isogeometric context is presented in [22]. The row vector $\mathbf{G}_d = \{\mathbf{G}_{d,k}\}_{k=1}^{m_u+1}$ forms a combined expo-rational basis of local degree d, defined on the one-dimensional domain Φ.

The combined expo-rational basis possesses the following properties:

- basis functions constitute a partition of unity;
- basis functions are linearly independent;

- minimal support of the basis functions is ensured independently of the local degree;
- basis functions are locally symmetric on the uniform knot vector.

From the properties above it follows that the basis evaluation can be parallelized in the computations. Each local curve/surface covers one node, hence, the computations can be performed node by node separately. Parallelization and pre-evaluation of basis functions are possible and successfully implemented, but achieving maximum performance is beyond the scope of the current paper.

One-dimensional blending spline constructions, i.e. curves, can be evaluated, alternatively to (3), by the following matrix formulation

$$A(u) = \mathbf{G}_d(u)\,\mathbf{Q}, \tag{5}$$

where the set of control points $\mathbf{Q}$ forms an ordered set of Bézier local curves of degree d.

The derivative of the curve (5) can be found as

$$DA(u) = D\mathbf{G}_d(u)\,\mathbf{Q},$$

where

$$D\mathbf{G}_d = \{D\mathbf{G}_{d,k}\}_{k=1}^{m_u+1} = \{\{DB_k\, b_{d,a}(\omega_k) + B_k\, Db_{d,a}(\omega_k)\}_{a=0}^{d}\}_{k=1}^{m_u+1}. \tag{6}$$

Bivariate basis can be easily obtained by the product of univariate bases, evaluated along two orthogonal parameters u and v, $(u, v) \in \Theta = [0, 1]^2$.

$$G_{d,i}(u, v) = G_{d,k_u,a_u}(u)\, G_{d,k_v,a_v}(v), \tag{7}$$

where $G_{d,k_u,a_u}(u)$, $G_{d,k_v,a_v}(v)$ represent single combined expo-rational basis function evaluated in u or v direction, respectively, in accordance with formula (4), having local degree d (which is not necessary should be equivalent in both directions). Finally, the basis functions $G_{d,i}(u, v)$ assemble a row vector of bivariate combined expo-rational basis functions $\mathbf{G}_d(u, v) = \{G_{d,i}\}_{i=1}^{(m_u+1)(m_v+1)(d+1)^2}$. Alternatively, bearing in mind the hierarchical structure of blending splines, one can evaluate a set of bivariate basis functions under each local surface ℓ_k as follows

$$\mathbf{G}_{d,k}(u, v) = \{B_{k_u}(u)\, b_{d,a_u}(\omega_{k_u}(u))\, B_{k_v}(v)\, b_{d,a_v}(\omega_{k_v}(v))\}_{a_u,a_v=0}^{d}, \tag{8}$$

where the index k for bivariate case is a pair (k_u, k_v).

In (8) local indices a_u and a_v iterate $d + 1$ times each, therefore, a number of basis functions on one node is $(d + 1)^2$. A set of bivariate basis functions evaluated under one local surface ℓ_k by formula (8) is shown in Fig. 2.

In the isogeometric analysis context, both geometry and solution are represented by the same basis functions. We will represent an initial geometry (domain) as a linear combination of bivariate combined expo-rational functions and corresponding control points $\mathbf{Q} \in \mathbb{R}^2$, while the solution of the physical problem, described by variational formulation, will be solved via the same set of basis functions with aim to obtain a vector of coefficients, whose combination with basis functions gives a smooth solution.

3. Domain construction

It is common to use triangulation algorithms for mesh generation. There are effective algorithms for triangulation that are suitable for complex shaped domains in 2D, for example, Delaunay algorithm. Since for tensor product surface a mesh grid is defined as a tensor product of two knot vectors, it imposes additional restrictions on mesh generation.

In the case of tensor product surfaces, the standard technique for surface approximation, called L^2-projection [23], can be used straightforward for the mesh generation, when the target domain parameterization $\chi(u, v)$, $(u, v) \in \Theta = [0, 1]^2$, is given in such a way that the boundary $\partial\Theta$ is mapped onto the boundary Γ. This projection minimizes L^2-norm of the difference between the target function and its approximation. Hence, $\chi(u, v)$ is a mapping $\chi : \Theta \to \Omega$ whose discretized approximation $\chi_h(u, v)$ is expressed in terms of blending tensor product surface. The L^2-projection method can be used for both mesh generation and subsequent *hp*-refinement.

Without going into much detail, we write the L^2-projection method in the matrix form as follows

$$\int_{\Theta} \mathbf{G}_d^{\mathrm{T}}\mathbf{G}_d\, d\Theta\, \mathbf{Q} = \int_{\Theta} \chi\mathbf{G}_d^{\mathrm{T}}\, d\Theta, \tag{9}$$

where $\mathbf{G}_d$ is a row vector of combined expo-rational basis functions of local degree d, $\mathbf{Q} \subset \mathbb{R}^2$ is a column vector of coefficients to be found, and $\chi(u, v)$ is a given function. The final domain approximation can be written as a tensor product surface in the form

$$\chi_h = \mathbf{G}_d\,\mathbf{Q}. \tag{10}$$

An example of constructing the domain is demonstrated in Fig. 3. Here the parameterization of a quarter of an annular section is given. The result of the L^2-projection method (9) is a set of control points $\mathbf{Q}$ forming local Bézier surfaces,

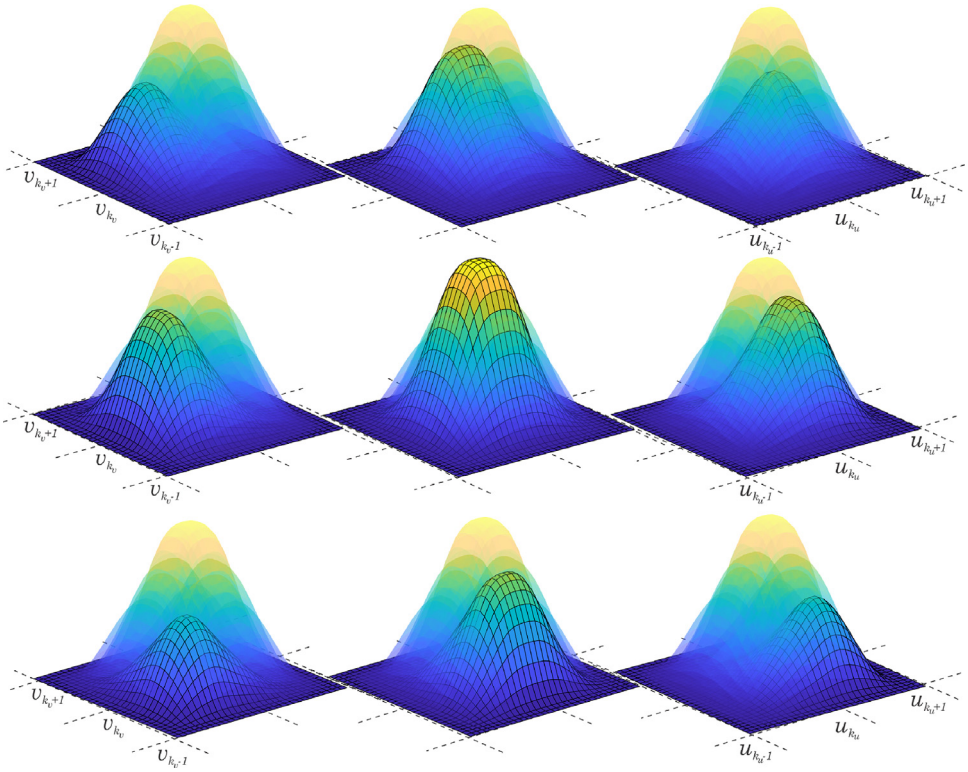

Fig. 2. A set of bivariate combined expo-rational basis functions $\mathbf{G}_{2,k}(u, v)$ defined on four neighbor elements $[u_{k_u-1}, u_{k_u+1}] \times [v_{k_v-1}, v_{k_v+1}]$ covered with one local surface ℓ_k, $k = (k_u, k_v)$.

whose blending gives the resulting domain χ_h (10). Fig. 4 shows the numerical convergence of the L^2-projection method of the surface approximation, shown in Fig. 3, with blending type surface construction. As one can see, the geometry error rapidly decreases with mesh refinement.

Alternatively, a *hp*-refinement scheme can be obtained by initializing the first coarse mesh manually. The blending splines provide a unique strategy for initial domain construction, which consists of a flexible arrangement of the initial local surfaces with successive mesh refinement.

Let $\chi_{h,0}$ be an initial coarse mesh, defined as

$$\chi_{h,0} = \mathbf{G}_{d_0}\mathbf{Q}_0,$$

where d_0 is an initial local degree and $\mathbf{Q}_0$ is a given column vector of points forming local Bézier surfaces. For example, if the initial mesh has size 2×2, nine local surfaces should be initialized, thus, for the local degree $d_0 = 1$, the vector $\mathbf{Q}_0$ contains 36 points.

In order to refine $\chi_{h,0}$, we evaluate new combined expo-rational basis $\mathbf{G}_d$ of local degree d on a new mesh and solve the following system of equations

$$\int_{\Theta} \mathbf{G}_d^{\mathrm{T}}\mathbf{G}_d \, d\Theta \, \mathbf{Q} = \int_{\Theta} \chi_{h,0}\mathbf{G}_d^{\mathrm{T}} \, d\Theta \tag{11}$$

or, in the matrix form

$$\mathcal{M}\,\mathbf{Q} = b.$$

A new blending tensor product surface $\chi_h = \mathbf{G}_d\,\mathbf{Q}$ approximates the initial coarse mesh $\chi_{h,0}$. An example of manual mesh initializing and its refinement is shown in Figs. 5 and 6, respectively. The uniqueness of this method is that the local surfaces can be oriented separately from each other yielding flexibility for both boundary construction and inner parameterization. While refinement occurs, the locality of the construction is preserved. Thus, the blending structure possesses a strong opportunity for adaptive mesh refinement strategies to be developed.

Fig. 7 demonstrates the dependence between the number of elements (m) of the square mesh and the number of degrees of freedom (n) for the corresponding blending tensor product surface of the local degrees $d = 1, 2, \ldots, 5$. The number of degrees of freedom is equivalent to the cardinality of the set of basis functions $\mathbf{G}_d$, and, correspondingly, the

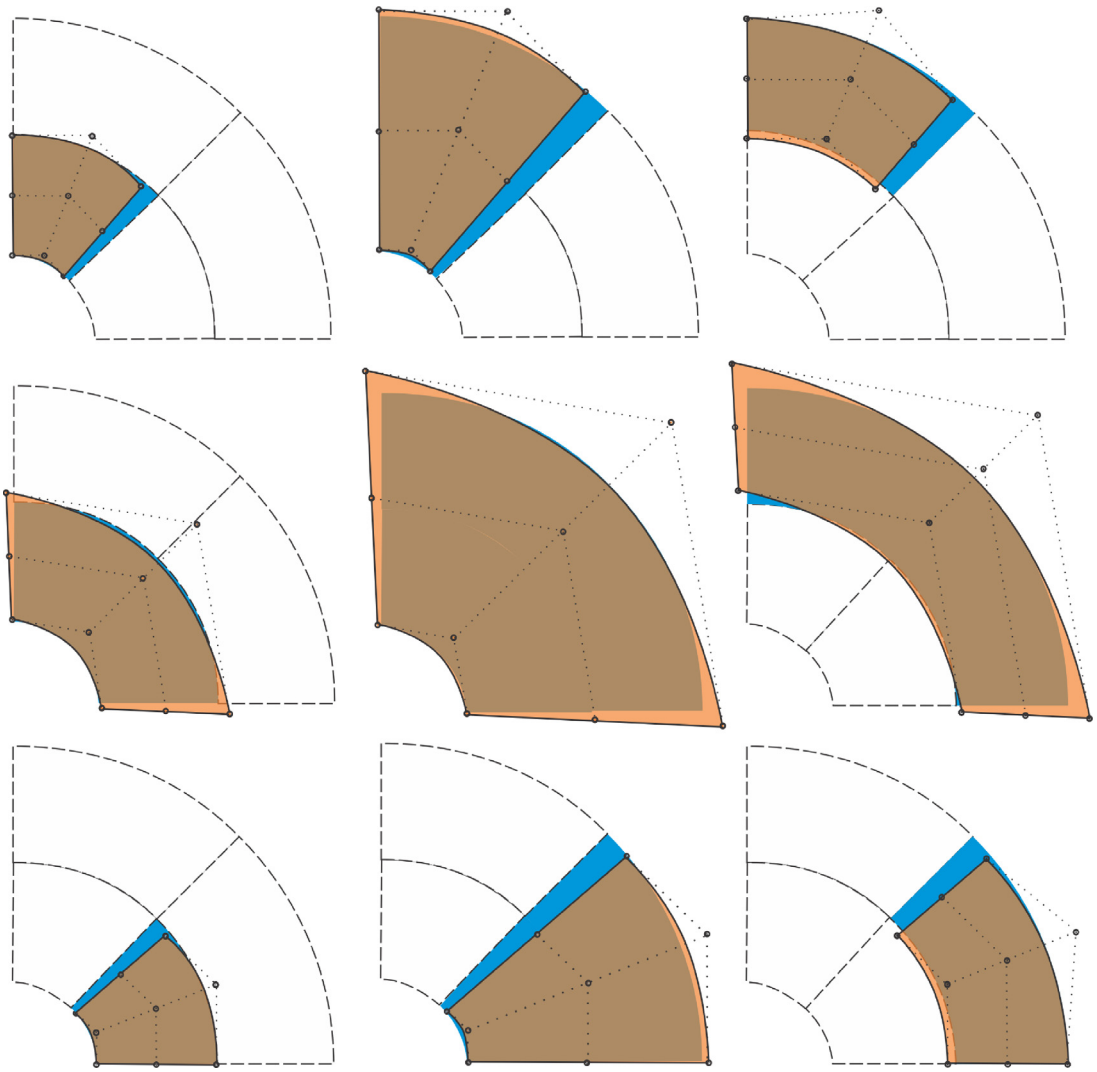

Fig. 3. An example of the domain approximation by using the combined expo-rational basis of local degree 2. The mesh of size 2×2 is obtained by the L^2-projection scheme. Nine Bézier local surfaces of the second degree are shown as orange surfaces with corresponding nets of control points. Each local surface affects some mesh elements, which are highlighted in blue color. Thus, each element is constructed by four overlapped local surfaces.

cardinality of the set of control points $\mathbf{Q}$, whose combination with basis functions gives a surface. Hence, the matrix $\mathcal{M}$ has size $n \times n$.

The hierarchical structure of the combined expo-rational basis leads to a specific form of stiffness, mass, and other similar matrices, which describe a physical system to be solved. Basis functions of each node contribute to the symmetric matrix block, whose set assembles a global matrix with predetermined structure always having block-tridiagonal form independently of the local degree. Schematically, the matrix $\mathcal{M}$ has the following form

$$\mathcal{M} = \begin{bmatrix} \mathcal{M}_{1,1} & \mathcal{M}_{2,1}^{\mathrm{T}} & 0 & \dots & 0 \\ \mathcal{M}_{2,1} & \mathcal{M}_{2,2} & \mathcal{M}_{3,2}^{\mathrm{T}} & \dots & 0 \\ 0 & \mathcal{M}_{3,2} & \mathcal{M}_{3,3} & & \vdots \\ \vdots & & & \ddots & \mathcal{M}_{m_u+1,m_u}^{\mathrm{T}} \\ 0 & \dots & & \mathcal{M}_{m_u+1,m_u} & \mathcal{M}_{m_u+1,m_u+1} \end{bmatrix}, \tag{12}$$

where $\mathcal{M}_{i,j}$ are the blocks of size $m_v + 1 \times m_v + 1$, $m_u m_v = m$ is a number of elements. Each block $\mathcal{M}_{i,j}$ also has block-tridiagonal form and consists of symmetric sub-blocks of size $(d+1)^2 \times (d+1)^2$ associated with particular basis functions, whose example is shown in Fig. 2. A specific example of the matrix $\mathcal{M}$ is shown in Fig. 8 for the mesh of size

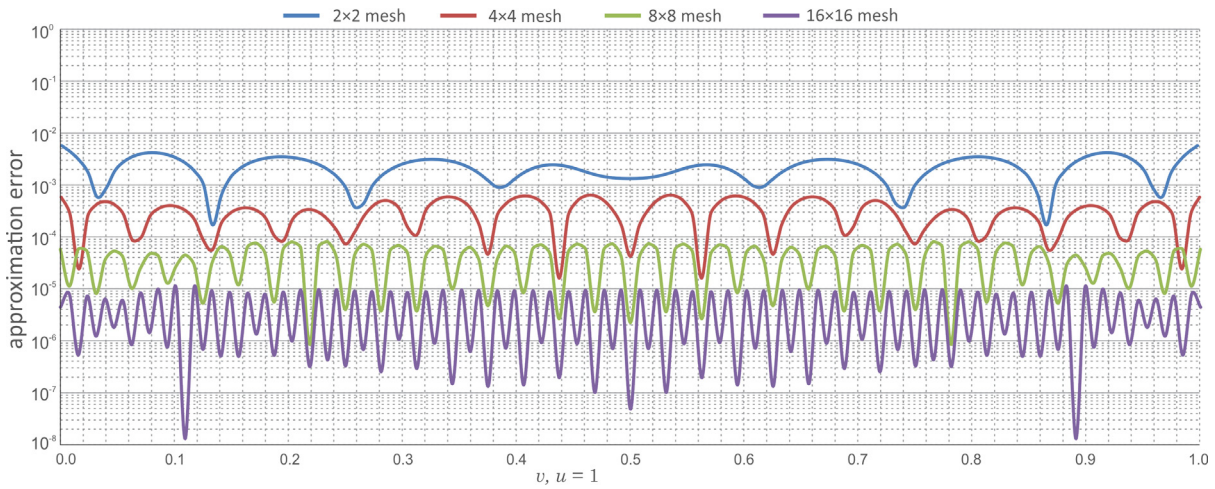

Fig. 4. Geometry error of the given domain shown in Fig. 3 approximated by the blending spline surface of the second degree. The error is computed as an absolute difference between the outer edge of the approximation ($u = 1$, $0 \le v \le 1$) and the exact outer radius of the domain. Four different meshes of size 2×2, 4×4, 8×8 and 16×16 are considered.

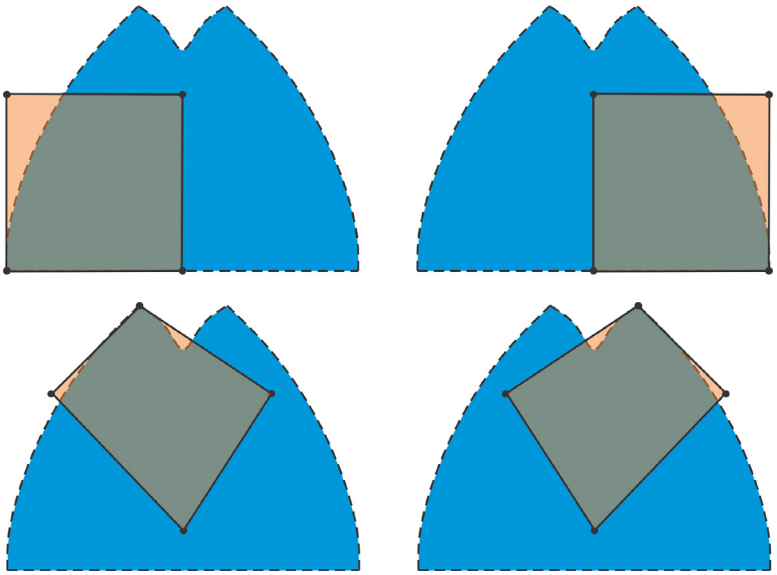

Fig. 5. An example of the initial domain consisted of one element and constructed manually by using four local surfaces of the first degree.

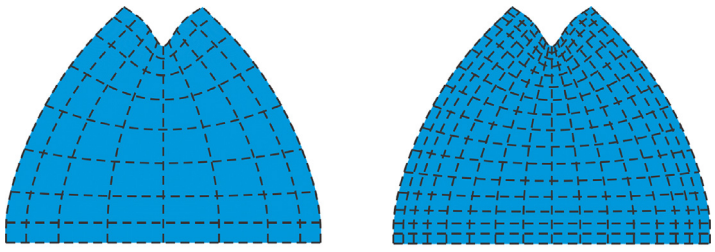

Fig. 6. Two refinements (a) 8×8 elements and (b) 16×16 elements of the initial mesh shown in Fig. 5 are obtained by the L^2-projection scheme.

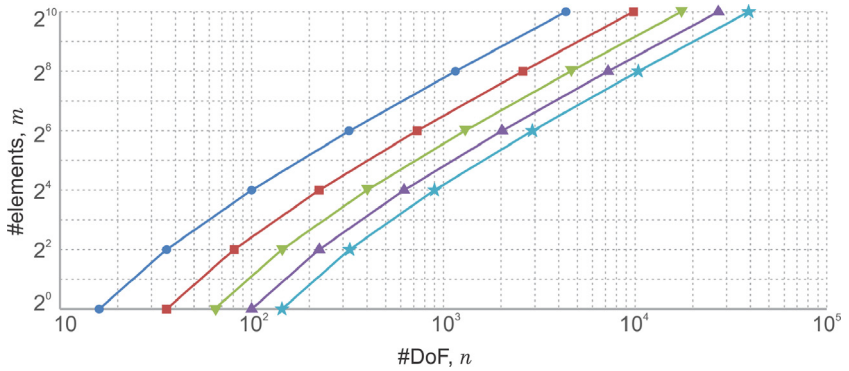

Fig. 7. Number of degrees of freedom (n) versus number of elements (m) for square 2D meshes with local degrees $d = 1, 2, \ldots, 5$ (●, ■, ▼, ▲, ★).

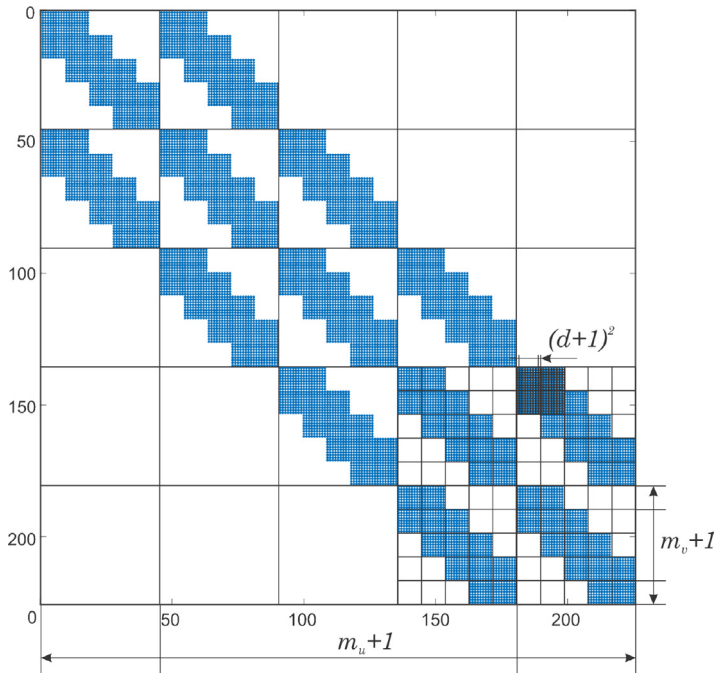

Fig. 8. The sparsity pattern of the matrix $\mathcal{M}$ for the mesh of size $m_u \times m_v = 4 \times 4$ and local degree $d = 2$.

$m_u \times m_v = 4 \times 4$ and local degree $d = 2$, where the size of each matrix block is demonstrated. The hierarchical structure of the matrix $\mathcal{M}$ provides opportunity to parallelize the computational process in such a way that contribution of each node can be computed separately of others. Parallelization can be useful for complex cases, for instance, with non-uniform knot distribution, or for local refinement schemes.

4. Isogeometric analysis

Many physical problems described by partial differential equations can be addressed by solving a variational problem. The isogeometric finite element method can be formulated in a very general framework. Let $\Omega \subset \mathbb{R}^2$ be a computational domain parameterized by planar blending tensor product surface with boundary Γ. As an illustrative example we consider the Poisson's equation

$$-\Delta\vartheta = f, \quad \text{in } \Omega, \tag{13}$$

with generalized boundary conditions, called Robin boundary conditions,

$$\nabla\vartheta \cdot \bar{n} = \kappa(\vartheta - g_D) - g_N, \quad \text{on } \Gamma, \tag{14}$$

where g_D and g_N are given functions, and κ is a constant that specify boundary conditions to be a Neumann or Dirichlet type. A large κ leads to the Dirichlet boundary conditions, while $\kappa = 0$ yields the Neumann boundary conditions.

To define the variational formulation of the problem, we introduce the trial and test spaces

$$\Upsilon_g = \{\vartheta \,:\, \vartheta \in H^1(\Omega),\ \vartheta|_\Gamma = g_D\},$$

$$\Upsilon = \{\upsilon \,:\, \upsilon \in H^1(\Omega),\ \upsilon|_\Gamma = 0\}.$$

Multiplying (13) with a test function $\upsilon \in \Upsilon$ and integrating by Green's formula, we obtain the following variational formulation: find $\vartheta \in \Upsilon_g$ such that $\upsilon \in \Upsilon$ and

$$\int_\Omega \nabla\vartheta \cdot \nabla\upsilon \, d\Omega + \kappa \int_\Gamma \vartheta\upsilon \, d\Gamma = \int_\Omega f\upsilon \, d\Omega + \int_\Gamma (\kappa g_D + g_N)\upsilon \, d\Gamma. \tag{15}$$

The blending spline basis functions form a set of finite-dimensional approximations of the test and trial spaces. The mesh is defined as a tensor product surface $\chi_h : \Theta \to \Omega$ consisted of $m = m_u m_v$ curvilinear elements. To compute the finite element approximation ϑ_h let $\mathbf{G}_d = \{G_{d,i}(u, v)\}_{i=1}^n$ be a basis defined on the parametric domain $\Theta = [0, 1]^2$ with n combined expo-rational basis functions of local degree d defined by formula (7). Applying the key idea of the isogeometric analysis, we represent the discrete solution field ϑ_h in a blending spline form, that is,

$$\vartheta_h = \sum_{i=1}^{n} G_{d,i}(u, v)\zeta_i = \mathbf{G}_d \, \zeta, \tag{16}$$

where ζ_i, $i = 1, \ldots, n$, are unknown coefficients to be found.

The discrete test functions υ_h are defined as

$$\upsilon_h = G_j(u, v), \quad j = 1, \ldots, n. \tag{17}$$

Substituting (16) and (17) into the variational formulation (15) we define a system of n PDEs for n coefficients ζ_i, $i = 1, \ldots, n$. In the matrix form we write this as

$$(\mathcal{A} + \kappa \, \mathcal{R})\zeta = b + r, \tag{18}$$

where the entries of the $n \times n$ stiffness matrix $\mathcal{A}$ and the $n \times 1$ force (load) vector b are defined as

$$\mathcal{A} = \int_\Omega \nabla\mathbf{G}_d^{\mathrm{T}} \nabla\mathbf{G}_d \, dxdy, \tag{19}$$

$$b = \int_\Omega f \, \mathbf{G}_d^{\mathrm{T}} \, dxdy. \tag{20}$$

The assembled stiffness matrix has a special form, which is similar to (12). Due to the tensor product representation, the stiffness matrix can be assembled for the entire set of basis functions simultaneously, without dividing it into elements. However, in order to keep parallelization of the computational process, one can conduct computations isolated for each local surface ℓ_k, or, in terms of finite elements, for each node.

Since the basis functions are defined on the parametric domain Θ, we need to determine the gradient $\nabla\mathbf{G}_d$ and the differential element of area $dxdy$ in the global coordinate system. The generalized approach of deriving the stiffness and mass matrices for curvilinear elements is detailed in [24,25]. We apply such an approach to blending spline finite elements without loss of generality.

The mapping of local parameters (u, v) onto global coordinates (x, y) is given by

$$x = \mathbf{G}_d \, \mathbf{Q}^x, \quad y = \mathbf{G}_d \, \mathbf{Q}^y,$$

where $\mathbf{Q} = \begin{bmatrix}\mathbf{Q}^x & \mathbf{Q}^y\end{bmatrix}$ is a column vector of control points of all the local surfaces with corresponding x- and y-components.

The partial derivatives of each basis function $G_{d,i}(u, v)$ with respect to the global coordinate system can be determined using the chain rule as follows

$$\frac{\partial G_{d,i}}{\partial x} = \frac{\partial G_{d,i}}{\partial u}\frac{\partial u}{\partial x} + \frac{\partial G_{d,i}}{\partial v}\frac{\partial v}{\partial x}, \quad \frac{\partial G_{d,i}}{\partial y} = \frac{\partial G_{d,i}}{\partial u}\frac{\partial u}{\partial y} + \frac{\partial G_{d,i}}{\partial v}\frac{\partial v}{\partial y}. \tag{21}$$

Expressions (21) can be rewritten in the matrix form for the entire set of basis functions

$$\begin{bmatrix} D_x\mathbf{G}_d \\ D_y\mathbf{G}_d \end{bmatrix} = J^{-1} \begin{bmatrix} D_u\mathbf{G}_d \\ D_v\mathbf{G}_d \end{bmatrix}, \tag{22}$$

where J is the Jacobi matrix, defined as

$$J = \begin{bmatrix} \dfrac{\partial x}{\partial u} & \dfrac{\partial y}{\partial u} \\ \dfrac{\partial x}{\partial v} & \dfrac{\partial y}{\partial v} \end{bmatrix} = \begin{bmatrix} D_u\mathbf{G}_d \\ D_v\mathbf{G}_d \end{bmatrix} \mathbf{Q}.$$

The differential element of area can be shown to transform according to [26]

$$dxdy = |J|dudv. \tag{23}$$

Substituting (22) and (23) into (19) we obtain

$$\mathcal{A} = \int_0^1 \int_0^1 \left(J^{-1} \begin{bmatrix} D_\xi \mathbf{G}_d \\ D_\eta \mathbf{G}_d \end{bmatrix} \right)^{\mathrm{T}} \left(J^{-1} \begin{bmatrix} D_\xi \mathbf{G}_d \\ D_\eta \mathbf{G}_d \end{bmatrix} \right) |J| dudv. \tag{24}$$

Similar computational strategy is valid for the load vector b (20)

$$b = \int_0^1 f(u, v)\, \mathbf{G}_d^{\mathrm{T}}\, |J| dudv. \tag{25}$$

Note that all the given functions, such as the external force f and similar, should be expressed in terms of parametric coordinates (u, v).

Now, we proceed to the Robin boundary conditions, defined as (14). This generalization of the boundary conditions leads to the following sparse boundary matrix $\mathcal{R}$ and boundary vector r

$$\mathcal{R} = \int_\Gamma \mathbf{G}_d^{\mathrm{T}} \mathbf{G}_d\, ds, \tag{26}$$

$$r = \int_\Gamma (\kappa g_D + g_N)\, \mathbf{G}_d^{\mathrm{T}}\, ds. \tag{27}$$

The boundary matrix and vector imply computations of curvilinear integrals along each boundary edge. Due to the agreement given in Section 3, the boundary of the parametric domain $\partial\Theta$ is projected onto the real boundary Γ. Then, we define the boundaries as a mapping of one of the parameters (u, v), while the other one is fixed, onto (x, y)

$$\begin{aligned} \Gamma = \{\gamma_1, \gamma_2, \gamma_3, \gamma_4\} = \{&\mathbf{G}_d(u, v = 0)\,\mathbf{Q},\ \mathbf{G}_d(u = 1, v)\,\mathbf{Q},\\ &\mathbf{G}_d(u, v = 1)\,\mathbf{Q},\ \mathbf{G}_d(u = 0, v)\,\mathbf{Q}\}. \end{aligned}$$

Corresponding derivatives along edges are denoted as

$$\begin{aligned} D\Gamma = \{D\gamma_1, D\gamma_2, D\gamma_3, D\gamma_4\} = \{&D_u\mathbf{G}_d(u, v = 0)\,\mathbf{Q},\ D_v\mathbf{G}_d(u = 1, v)\,\mathbf{Q},\\ &D_u\mathbf{G}_d(u, v = 1)\,\mathbf{Q},\ D_v\mathbf{G}_d(u = 0, v)\,\mathbf{Q}\}. \end{aligned}$$

Then, the boundary matrix $\mathcal{R}$ (26) can be expressed as

$$\mathcal{R} = \sum_{\iota=1}^{4} \int_{\gamma_\iota} \kappa \mathbf{G}_d^{\mathrm{T}} \mathbf{G}_d\, ds = \sum_{\iota=1}^{4} \int_0^1 \kappa \mathbf{G}_d\big|_{\gamma_\iota}^{\mathrm{T}} \mathbf{G}_d\big|_{\gamma_\iota} \sqrt{(D\gamma_\iota^x)^2 + (D\gamma_\iota^y)^2}\, dw, \tag{28}$$

where the basis functions $\mathbf{G}_d\big|_{\gamma_\iota}$ are defined on the respective boundary edge, $D\gamma_\iota^x$ and $D\gamma_\iota^y$ are the corresponding x- and y-coordinates of the boundary derivative, and w is a formal parameter, which is u or v depending on the boundary index.

The entries of the boundary vector r (27) can be transformed as

$$r = \sum_{\iota=1}^{4} \int_{\gamma_\iota} (\kappa g_D + g_N) \mathbf{G}_d^{\mathrm{T}}\, d\gamma_\iota = \sum_{\iota=1}^{4} \int_0^1 (\kappa g_D + g_N) \mathbf{G}_d\big|_{\gamma_\iota}^{\mathrm{T}} \sqrt{(D\gamma_\iota^x)^2 + (D\gamma_\iota^y)^2}\, dw. \tag{29}$$

Substituting (24), (25), (28) and (29) into (18) and solving this matrix equation, we finally obtain a discrete solution of the Poisson's equation in the following form

$$\vartheta_h = \mathbf{G}_d\, \zeta\,.$$

5. Numerical examples

The numerical examples below demonstrate the main features of the blending splines in application to the isogeometric analysis. We consider the specific approaches to the construction of 2D domains, approximation of the boundary conditions, and the convergence rate of the proposed method. A comparison of the proposed method with the NURBS-based isogeometric approach is not straightforward due to the inconsistency in the number of degrees of freedom in both cases, as well as the lack of strict locality in the NURBS case with increasing the spline degree. However, conversion between both the bases is supported, and the corresponding research can be found in [22], where the blending spline basis and the B-spline basis are compared locally.

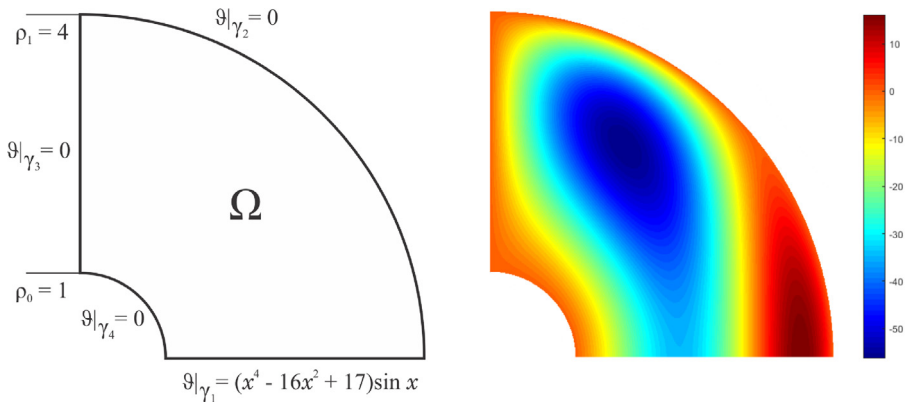

Fig. 9. Geometry, boundary conditions and exact solution of the Poisson's equation example.

5.1. Poisson's equation

To illustrate the blending-spline-based finite element method, we consider a test problem with a known solution. As shown in Fig. 9, the given domain Ω is bounded by the quarter annulus, located within the positive quadrant of the Cartesian coordinate system. A boundary Γ consists of four edges $\Gamma = \{\gamma_1, \gamma_2, \gamma_3, \gamma_4\}$.

A model problem is a Poisson's equation given by

$$-\Delta\vartheta = f, \quad \text{in } \Omega, \tag{30}$$

the boundary conditions are

$$\begin{cases} \vartheta = g_D, & \text{on } \gamma_1, \\ \vartheta = 0, & \text{on } \gamma_2,\ \gamma_3,\ \gamma_4, \end{cases} \tag{31}$$

where $g_D = (x^4 - 16x^2 + 17)\sin x$.

We define the load f in such a way that the exact solution reads

$$\vartheta = (\rho^2 - 1)(\rho^2 - 16)\sin x,$$

where $\rho = \sqrt{x^2 + y^2}$. The exact solution is shown in Fig. 9.

We first construct a mesh as the L^2-projection of the given domain parameterization onto the discretized finite element space of blending splines. An example of the mesh generation by the L^2-projection method is shown in Fig. 3. The domain parameterization is given as

$$\chi(u, v) = \begin{cases} \rho\cos\phi \\ \rho\sin\phi \end{cases} = \begin{cases} (3u+1)\cos\frac{\pi}{2}v \\ (3u+1)\sin\frac{\pi}{2}v. \end{cases} \tag{32}$$

Let $\mathbf{G}_d(u, v)$ be a combined expo-rational basis of local degree d evaluated on a mesh constructed by a tensor product of two uniform knot vectors defined along two orthogonal parameters u and v. A mesh width h is defined as a distance between two neighbor knots. A column vector of control points $\mathbf{Q}$ can be found by the L^2-projection scheme (9) by substituting the given $\chi(u, v)$ (32).

The finite element method for the problem (30)–(31) can be formulated as follows

$$\left(\int_\Omega \nabla\mathbf{G}_d^{\mathrm{T}}\nabla\mathbf{G}_d\, d\Omega + \kappa\int_\Gamma \mathbf{G}_d^{\mathrm{T}}\mathbf{G}_d\, d\Gamma\right)\zeta = \int_\Omega f\,\mathbf{G}_d^{\mathrm{T}}\, d\Omega + \int_{\partial\Omega}\kappa g_D\,\mathbf{G}_d^{\mathrm{T}}\, d\Gamma, \tag{33}$$

where κ is a constant which affects the type of the boundary conditions. Sufficiently high κ gives the Dirichlet boundary conditions.

In the compact matrix form (33) can be rewritten as

$$(\mathcal{A} + \kappa\mathcal{R})\zeta = b + r, \tag{34}$$

where $\mathcal{A}$ is a stiffness matrix, b is a force vector, $\mathcal{R}$ and r are the boundary matrix and vector, respectively. A transformation between the parametric domain Θ and the real domain Ω is performed in accordance with formulas (24), (25), (28) and (29). After solving the matrix equation (34), we express the solution as

$$\vartheta_h = \mathbf{G}_d\,\zeta.$$

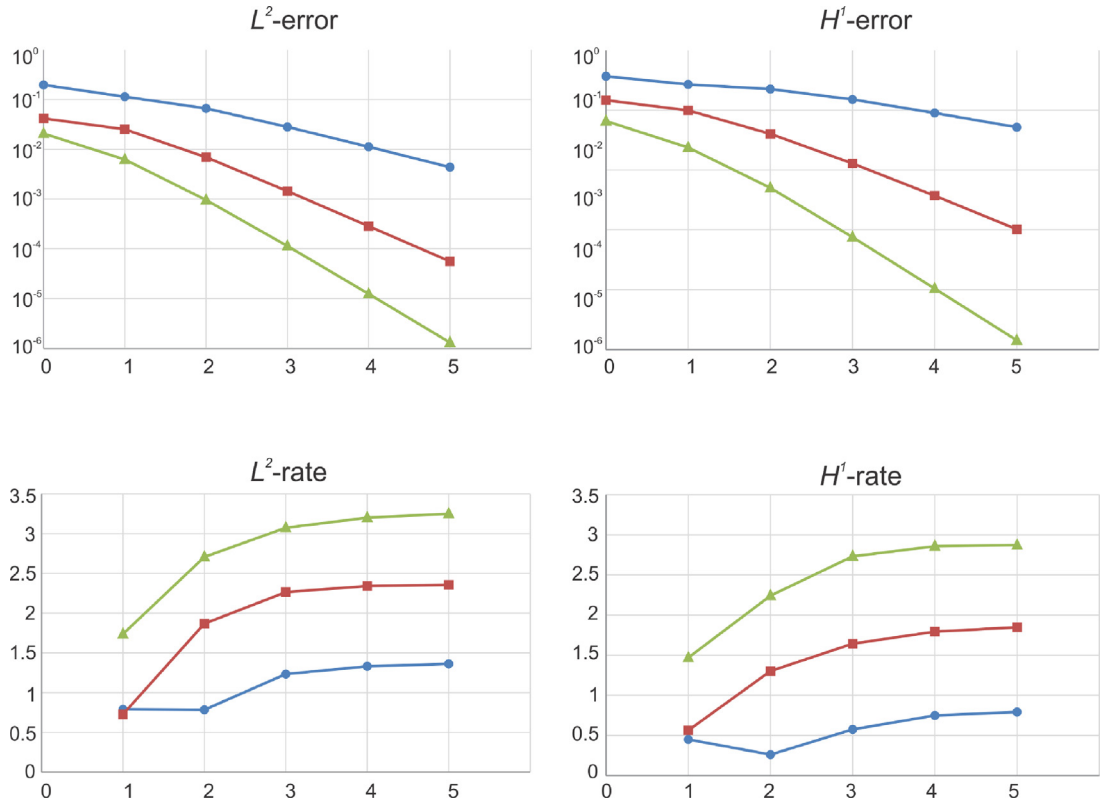

Fig. 10. Errors $\|e_h\|_{L^2}$ and $\|e_h\|_{H^1}$ (top) and convergence rates (bottom) for blending spline approximations of local degrees $d = 1, 2, 3$ (●, ■, ▲) and grid width $h = 2^{-\mu}$, $\mu = 0, 1, \ldots, 5$.

We compute errors of the blending spline approximations obtained on the tensor product mesh with grid width h in two norms: L^2-norm

$$\|e_h\|_{L^2} = \left(\int_\Omega |\vartheta_h - \vartheta|^2 d\Omega \right)^{\frac{1}{2}} \tag{35}$$

and H^1-norm

$$\|e_h\|_{H^1} = \left(\int_\Omega \left(|\vartheta_h - \vartheta|^2 + |\nabla\vartheta_h - \nabla\vartheta|^2 \right) d\Omega \right)^{\frac{1}{2}}, \tag{36}$$

where ϑ is an exact solution of the considered problem and ϑ_h is an approximated solution.

In order to demonstrate the convergence rate, we use the following formula

$$r_{(\cdot)} = \log_2 \left(\frac{\|e_h\|_{(\cdot)}}{\|e_{h/2}\|_{(\cdot)}} \right), \tag{37}$$

where $(\cdot)$ defines L^2- or H^1-norm.

Fig. 10 visualizes the error of blending spline approximations. In the top two diagrams, errors $\|e_h\|_{L^2}$ (35) and $\|e_h\|_{H^1}$ (36) are plotted versus the grid width h for local degrees $d = 1, 2, 3$. The bottom diagrams show the numerically computed convergence rates (37).

The approximations maintain the local representation independently of the local degree d. However, a higher degree gives better approximation and faster convergence.

5.2. Helmholtz equation

In the second example we consider the Helmholtz equation defined on a convex hexagon domain. When high wave numbers or highly oscillatory solutions occur, it becomes a challenge to achieve reasonable accuracy, namely, for the linear elements the element size is required to be less than 1/10th of the minimum wavelength [27]. This problem has been studied, for instance, in [28,29].

The Helmholtz equation is typical of the form

$$-\Delta\vartheta - k^2\vartheta = f, \quad \text{in } \Omega, \tag{38}$$

where k is the wave number, f represents a harmonic source. We involve the following Robin boundary conditions

$$\nabla\vartheta \cdot \bar{n} - ik\vartheta = g, \quad \text{on } \Gamma. \tag{39}$$

In our particular case $f = \sin(k\rho)/\rho$, where $\rho = \sqrt{x^2 + y^2}$, and the boundary data g is chosen so that the exact solution reads

$$\vartheta = \frac{\cos(k\rho)}{k} - \frac{\cos k + i \sin k}{k(J_0(k) + iJ_1(k))} J_0(k\rho),$$

where $J_i(z)$ are Bessel functions of the first kind.

We construct a mesh by manual initialization of initial local surfaces. A coarse 2×2 mesh requires 9 local surfaces located in such a way that the hexagon domain is constructed. One can manipulate with inner domain parameterization by adjustment of control points. We start with the first degree and then automatically refine local surfaces to a higher degree by using the L^2-projection method (11). Since the purpose of this example is to show the high local degree approximation, we refine mostly the local degree, not the mesh grid.

The finite element method for the problem (38)–(39) is formulated as

$$\left(\int_\Omega \nabla \mathbf{G}_d^{\mathrm{T}} \nabla \mathbf{G}_d \, d\Omega - k^2 \int_\Omega \mathbf{G}_d^{\mathrm{T}} \mathbf{G}_d \, d\Omega - ik \int_\Gamma \mathbf{G}_d^{\mathrm{T}} \mathbf{G}_d \, d\Gamma \right) \zeta = \int_\Omega f \, \mathbf{G}_d^{\mathrm{T}} \, d\Omega + \int_\Gamma g \, \mathbf{G}_d^{\mathrm{T}} \, d\Gamma. \tag{40}$$

Rewriting (40) in the compact matrix form, we obtain

$$(\mathcal{A} - k^2\mathcal{M} - ik\mathcal{R})\zeta = b + r. \tag{41}$$

We solve the system (41) with respect to the column vector of coefficients ζ, involving coordinate transformation between the parametric domain Θ and the real domain Ω. Finally, a linear combination of the basis functions $\mathbf{G}_d$ and complex coefficients ζ gives us an approximated solution of the Helmholtz equation.

Fig. 11 demonstrates the approximated solution for the problem (38)–(39) with $k = 20$. Two coarse meshes are considered: 2×2 and 4×4. The solution is approximated by blending tensor product surfaces of two local degrees: $d = 4$ and $d = 7$. Another example, see Fig. 12, presents the blending surface approximation when applied to a challenging case of high wave number. Here we take $k = 50$, uniform mesh of size 8×8 and local degree $d = 10$. One can see that the numerical result with the coarse mesh captures the oscillation of the exact solution very well. We leave a deeper analysis of the application of blending spline construction to the Helmholtz problem for future research when we will investigate adaptive mesh refinement schemes.

Comparing theoretically isogeometric approach based on B-splines with an alternative isogeometric approach, which is based on blending spline construction, one can realize the differences between them. The B-spline basis function of degree p covers $p + 1 \times p + 1$ elements. For a high degree and a coarse mesh this leads to the globality of the basis. Maintaining locality, the blending spline construction is more beneficial for high frequency approximation in terms of computations, because each node can be treated independently of each other. Moreover, there is a strong opportunity to develop an adaptive curvilinear grid for blending spline construction by flexible manipulating with inner parameterization, which can improve the final approximation. Also, the strict locality allows for local refinement by knot insertion maintaining minimal support of basis functions independently of the local degree. Alternatively, the local degree refinement can handle local oscillations without affecting the rest of the domain. We believe that mesh adaptability can give a much better result in terms of the convergence rate in future development.

5.3. Linear elasticity problem

We now consider the problem of linear elastostatics. For more details regarding the derivation of the partial differential equation governing linear elasticity, we refer to [23,30].

Let the vector ϑ be a displacement $\vartheta = (\vartheta_1, \vartheta_2) = \bar{x} - \bar{x}_0$, where $\bar{x}$ is a current position of some material particle and $\bar{x}_0$ is an initial position.

The strain tensor is defined as

$$\varepsilon = \frac{1}{2}(\nabla\vartheta + \nabla\vartheta^{\mathrm{T}}).$$

The strain and stress relation takes the form

$$\sigma = 2\mu\varepsilon(\vartheta) + \lambda(\nabla \cdot \vartheta)I_2, \tag{42}$$

where I_2 is the 2×2 identity matrix. The Lamé parameters μ and λ are defined by

$$\mu = \frac{E}{2(1+\nu)}, \quad \lambda = \frac{E\nu}{(1+\nu)(1-2\nu)},$$

where E is Young's elastic modulus and ν is Poisson's ratio.

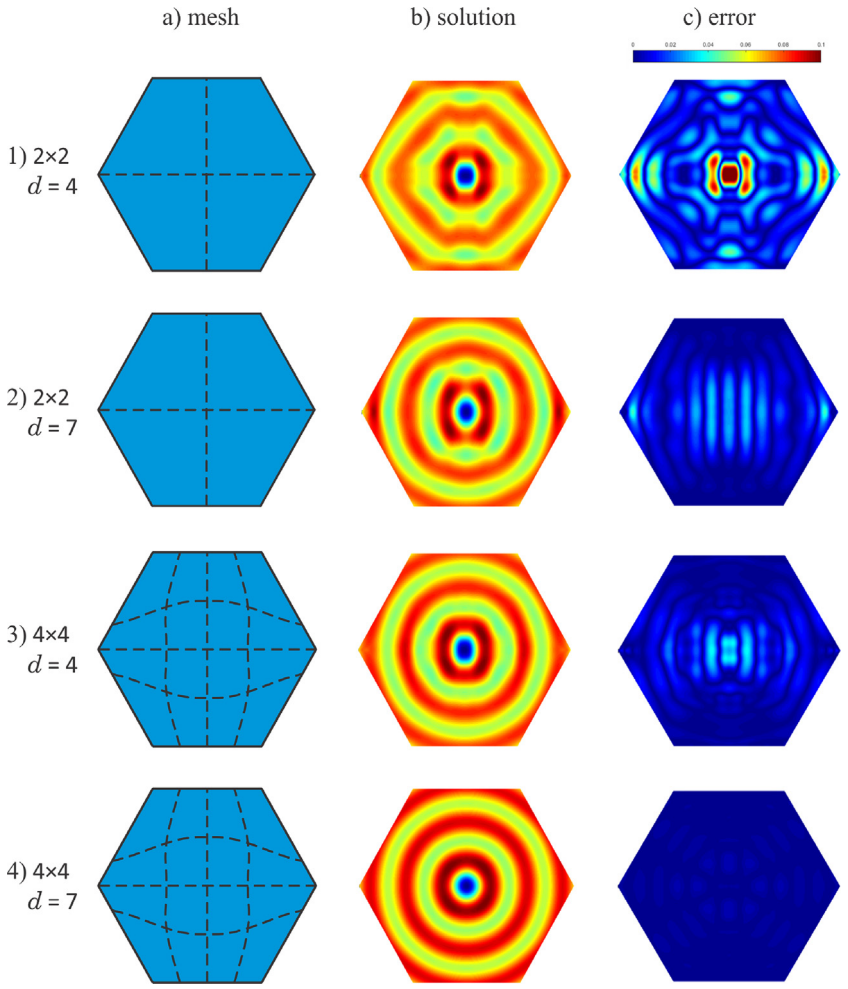

Fig. 11. Two meshes, two local degrees, corresponding solutions and absolute errors for the Helmholtz problem.

The basic problem of linear elastostatics is to find the stress tensor σ and the displacement vector ϑ such that

$$-\nabla\cdot\sigma(\vartheta)=0,\quad \text{in } \Omega, \tag{43a}$$

$$\sigma(\vartheta)\cdot\bar{n}=g_N,\quad \text{on } \Gamma_N, \tag{43b}$$

$$\vartheta=g_D,\quad \text{on } \Gamma_D. \tag{43c}$$

Let us introduce the Robin boundary conditions that cover both Neumann (43b) and Dirichlet (43c) boundary conditions as

$$-\sigma(\vartheta)\cdot\bar{n}=\kappa(\vartheta-g_D)-g_N,\quad \text{on } \Gamma=\Gamma_D\cup\Gamma_N, \tag{44}$$

where κ is a constant determining the Dirichlet or Neumann type of the boundary conditions.

Let the initial domain be approximated by the blending tensor product surface as

$$\chi_h=\mathbf{G}_d\,\mathbf{Q},$$

where $\mathbf{G}_d$ is a combined expo-rational basis, constructed on a given mesh, and $\mathbf{Q}$ is a column vector of control points obtained, for example, by the L^2-projection method, recall (9).

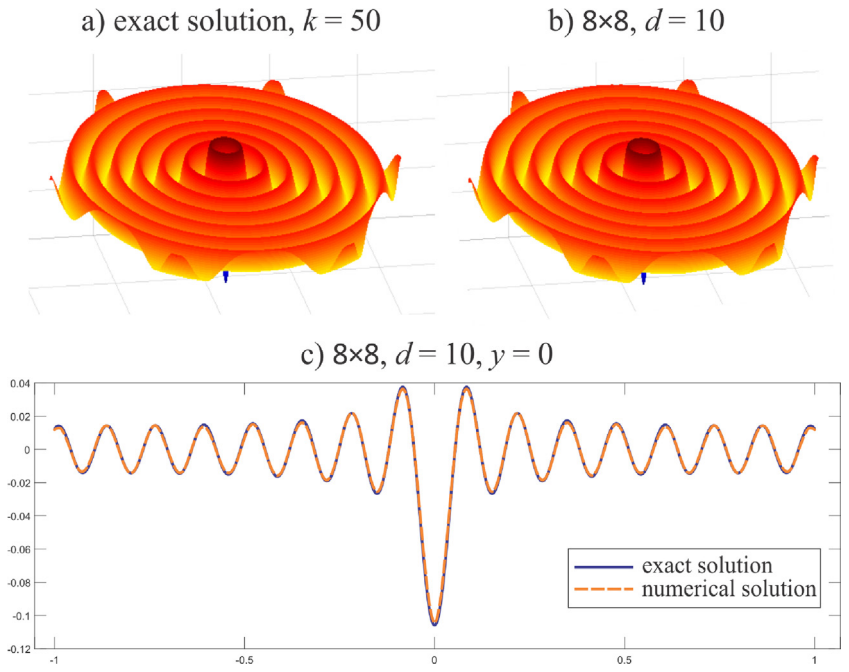

Fig. 12. (a) Exact solution, $k = 50$. (b) Blending tensor product surface approximation for 8×8 mesh and local degree $d = 10$. (c) The trace plot along x-axis.

Using engineering notations, we write the discrete solution ϑ_h in matrix form as

$$\vartheta_h = \begin{bmatrix} (\vartheta_h)_1 \\ (\vartheta_h)_2 \end{bmatrix} = \begin{bmatrix} G_{d,1} & 0 & G_{d,2} & 0 & \dots & G_{d,n} & 0 \\ 0 & G_{d,1} & 0 & G_{d,2} & \dots & 0 & G_{d,n} \end{bmatrix} \begin{bmatrix} \zeta_{11} \\ \zeta_{21} \\ \zeta_{12} \\ \zeta_{22} \\ \vdots \\ \zeta_{1n} \\ \zeta_{2n} \end{bmatrix} = \mathbf{G}_d\, \zeta\,. \tag{45}$$

The relation (42) can be expressed as

$$\sigma = \mathcal{D}\varepsilon,$$

where

$$\mathcal{D} = \begin{bmatrix} \lambda + 2\mu & \lambda & 0 \\ \lambda & \lambda + 2\mu & 0 \\ 0 & 0 & \mu \end{bmatrix}.$$

The strain ε is linked to the displacements ϑ by

$$\begin{bmatrix} \varepsilon_{11} \\ \varepsilon_{22} \\ 2\varepsilon_{12} \end{bmatrix} = \begin{bmatrix} \partial\vartheta_1/\partial x \\ \partial\vartheta_2/\partial y \\ \partial\vartheta_1/\partial y + \partial\vartheta_2/\partial x \end{bmatrix} = \begin{bmatrix} \partial/\partial x & 0 \\ 0 & \partial/\partial y \\ \partial/\partial y & \partial/\partial x \end{bmatrix} \begin{bmatrix} \vartheta_1 \\ \vartheta_2 \end{bmatrix} =$$

$$= \begin{bmatrix} \partial/\partial x & 0 \\ 0 & \partial/\partial y \\ \partial/\partial y & \partial/\partial x \end{bmatrix} \begin{bmatrix} G_{d,1} & 0 & G_{d,2} & 0 & \dots & G_{d,n} & 0 \\ 0 & G_{d,1} & 0 & G_{d,2} & \dots & 0 & G_{d,n} \end{bmatrix} \begin{bmatrix} \zeta_{11} \\ \zeta_{21} \\ \zeta_{12} \\ \zeta_{22} \\ \vdots \\ \zeta_{1n} \\ \zeta_{2n} \end{bmatrix}. \tag{46}$$

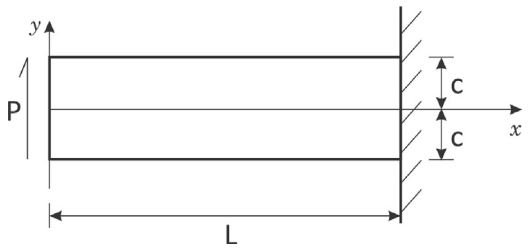

Fig. 13. Geometry of the cantilever beam.

We now need to express partial derivatives $\partial/\partial x$ and $\partial/\partial y$ in terms of the parameters u and v. We know, recall (21), that

$$\frac{\partial}{\partial x} = \frac{\partial}{\partial u}\frac{\partial u}{\partial x} + \frac{\partial}{\partial v}\frac{\partial v}{\partial x}, \qquad \frac{\partial}{\partial y} = \frac{\partial}{\partial u}\frac{\partial u}{\partial y} + \frac{\partial}{\partial v}\frac{\partial v}{\partial y}.$$

Thus,

$$\begin{bmatrix} \partial/\partial x & 0 \\ 0 & \partial/\partial y \\ \partial/\partial y & \partial/\partial x \end{bmatrix} = \begin{bmatrix} \partial u/\partial x & 0 & \partial v/\partial x & 0 \\ 0 & \partial u/\partial y & 0 & \partial v/\partial y \\ \partial u/\partial y & \partial u/\partial x & \partial v/\partial y & \partial v/\partial x \end{bmatrix} \begin{bmatrix} \partial/\partial u & 0 \\ 0 & \partial/\partial u \\ \partial/\partial v & 0 \\ 0 & \partial/\partial v \end{bmatrix}. \tag{47}$$

Substituting (47) into (46) we introduce the strain matrix

$$\mathcal{B} = \begin{bmatrix} \partial u/\partial x & 0 & \partial v/\partial x & 0 \\ 0 & \partial u/\partial y & 0 & \partial v/\partial y \\ \partial u/\partial y & \partial u/\partial x & \partial v/\partial y & \partial v/\partial x \end{bmatrix} \begin{bmatrix} D_u G_{d,1} & 0 & D_u G_{d,2} & 0 & \dots & D_u G_{d,n} & 0 \\ 0 & D_u G_{d,1} & 0 & D_u G_{d,2} & \dots & 0 & D_u G_{d,n} \\ D_v G_{d,1} & 0 & D_v G_{d,2} & 0 & \dots & D_v G_{d,n} & 0 \\ 0 & D_v G_{d,1} & 0 & D_v G_{d,2} & \dots & 0 & D_v G_{d,n} \end{bmatrix} \tag{48}$$

and obtain the discrete strain and stress

$$\varepsilon(\vartheta_h) = \begin{bmatrix} \varepsilon_{11}(\vartheta_h) \\ \varepsilon_{22}(\vartheta_h) \\ 2\varepsilon_{12}(\vartheta_h) \end{bmatrix} = \mathcal{B}\zeta, \tag{49}$$

$$\sigma(\vartheta_h) = \begin{bmatrix} \sigma_{11}(\vartheta_h) \\ \sigma_{22}(\vartheta_h) \\ \sigma_{12}(\vartheta_h) \end{bmatrix} = \mathcal{D}\mathcal{B}\zeta. \tag{50}$$

Using definitions (49) and (50) we obtain the following finite element method for the problem (43a), (44)

$$\left(\int_{\Theta} \mathcal{B}^{\mathrm{T}} \mathcal{D}\, \mathcal{B}\, |J|\, du dv + \kappa \int_{\Gamma} \mathbf{G}_d^{\mathrm{T}} \mathbf{G}_d\, d\Gamma \right) \zeta = \int_{\Gamma} (\kappa g_D + g_N)\, \mathbf{G}_d^{\mathrm{T}}\, d\Gamma. \tag{51}$$

where $\mathbf{G}_d$ is a set of combined expo-rational basis functions written in the special form as shown in formula (45), and g_D, g_N are vector functions $g_D = \begin{bmatrix} g_{D1} & g_{D2} \end{bmatrix}^{\mathrm{T}}$, $g_N = \begin{bmatrix} g_{N1} & g_{N2} \end{bmatrix}^{\mathrm{T}}$. Transformation between parametric and real domain is gained by Jacobian $|J|$, and curvilinear integrals, which are the entires of boundary integrals, are evaluated in accordance with formulas (28), (29).

Thus, the deformed mesh can be constructed as

$$\chi_h + \vartheta_h = \begin{bmatrix} G_{d,1} & G_{d,2} & \dots & G_{d,n} \end{bmatrix} \begin{bmatrix} q_1^x + \zeta_{11} & q_1^y + \zeta_{21} \\ q_2^x + \zeta_{12} & q_2^y + \zeta_{22} \\ \vdots & \\ q_n^x + \zeta_{1n} & q_n^y + \zeta_{2n} \end{bmatrix},$$

where $\begin{bmatrix} q_1^x & q_2^x & \dots & q_n^x \\ q_1^y & q_2^y & & q_n^y \end{bmatrix}^{\mathrm{T}} = \mathbf{Q}$ is a column vector of control points constructing the domain. In addition, strain and stress can be found by the formulas (49), (50), respectively.

In our particular example of the two-dimensional elasticity problem, we consider the bending of a cantilever beam loaded at the end. A model shown in Fig. 13 have a narrow rectangular cross-section of unit width bent by a force P

applied at the end $x = 0$. In accordance with [31], the stress field in the cantilever is given by

$$\sigma_{11} = -\frac{Pxy}{I}, \quad \sigma_{22} = 0, \quad \sigma_{12} = -\frac{P}{2I}\left(c^2 - y^2\right)$$

and the displacement field $\vartheta = (\vartheta_1, \vartheta_2)$ is

$$\vartheta_1 = -\frac{Px^2y}{2EI} - \frac{\nu Py^2}{6EI} + \frac{Py^3}{6IG} + \left(\frac{PL^2}{2EI} - \frac{Pc^2}{2IG}\right)y,$$
$$\vartheta_2 = \frac{\nu Pxy^2}{2EI} + \frac{Px^3}{6EI} - \frac{PL^2x}{2EI} + \frac{PL^3}{3EI},$$

where E is replaced as $\frac{E}{(1-\nu)^2}$, ν is replaced as $\frac{\nu}{1-\nu}$, $G = \frac{E}{2(1+\nu)}$, $I = \frac{2}{3}c^3$ is the moment of inertia of the cross section of the cantilever. In order to obtain precise approximation we set the exact solution $\vartheta = (\vartheta_1, \vartheta_2)$ as boundary conditions.

We approximate the domain by using the L^2-projection method, see (9). The cantilever beam is described by the following parameterization

$$\chi(u, v) = \begin{cases} Lu \\ c(2v - 1), \end{cases}$$

where $L = 8$, $c = 1$. For more uniform density of the mesh, let the number of elements along the parameter u be twice as large as the number of elements along the parameter v, i.e. $m_u = 2m_v$.

We define the combine expo-rational basis $\mathbf{G}_d$ on the mesh of size $2m_v \times m_v$ and solve system (51). The resulting vector ζ gives us the solution ϑ_h and the corresponding stress tensor $\sigma(\vartheta_h)$, shown in Fig. 14 for meshes (a) 2×1, (b) 8×4, (c) 32×16. Comparing with the exact solution shown in Fig. 14(d), one can see the convergence for stress components with mesh refinement.

6. Conclusion

In this paper, we demonstrated how the blending type spline construction can be applied to the isogeometric analysis. We described *h*-, *p*-, and *hp*-refinement schemes of the domains constructed with blending tensor product surfaces and explored their behavior on three numerical examples.

The first example is Poisson's equation with inhomogeneous Dirichlet boundary conditions. It was chosen to demonstrate the convergence of the proposed method. We studied *h*- and *p*-refinement schemes and compared L^2- and H^1-errors and convergence rates. The test has shown improving accuracy with both refinement schemes, while a strong locality of the representation is maintained.

In the second example, we considered the Helmholtz equation with a relatively large wave number for the mesh consisting of a few elements. In addition, manual domain construction and its refinement were demonstrated. The strong locality of blending splines facilitates the treatment of local singularities of the desired solution. We assume that there is an opportunity to improve the accuracy of the approximation by parameterization editing and mesh adaptation. This research question needs to be addressed in future work.

The third example shows how the different characteristics of the physical system (displacement, stress, and strain) are represented by the same basis functions in application to the elastostatic problem. We considered in detail the process of solving the linear elasticity problem and, in particular, applied the method to the bending of a cantilever beam loaded at the end. Uniform mesh refinement resulted in the improved approximation of the stress components.

In conclusion, our studies reveal the following items and features of the analysis framework based on the blending splines:

1. A mesh for a tensor product blending surface is defined by the product of knot vectors. Knot intervals subdivide the domain into elements.
2. The support of each basis function always consists of four elements, where the corresponding local surface is defined, i.e. the basis is strictly local.
3. The control points associated with the basis functions define the geometry. The same basis functions are used for representing the solution of the problem of interest.
4. A set of local surfaces provides an additional level of abstraction between control points and elements due to the multilayer structure. Local surfaces interpolate the finite elements while being constructed by control points. The finite elements are independent of each other and smoothly connected at the same time.
5. Adjustable mesh refinement can be achieved by knot insertion. New local surfaces can be expressed in terms of existing local surfaces.
6. Despite the use of standard FEM algorithms, which are common for any type of smooth basis, the solution obtained by employing the expo-rational basis approximation preserves the properties of blending surfaces, i.e. the spline structure stores many potentially useful intrinsic properties/inner information about the global geometry (for example, normals, curvature, torsion, etc.)

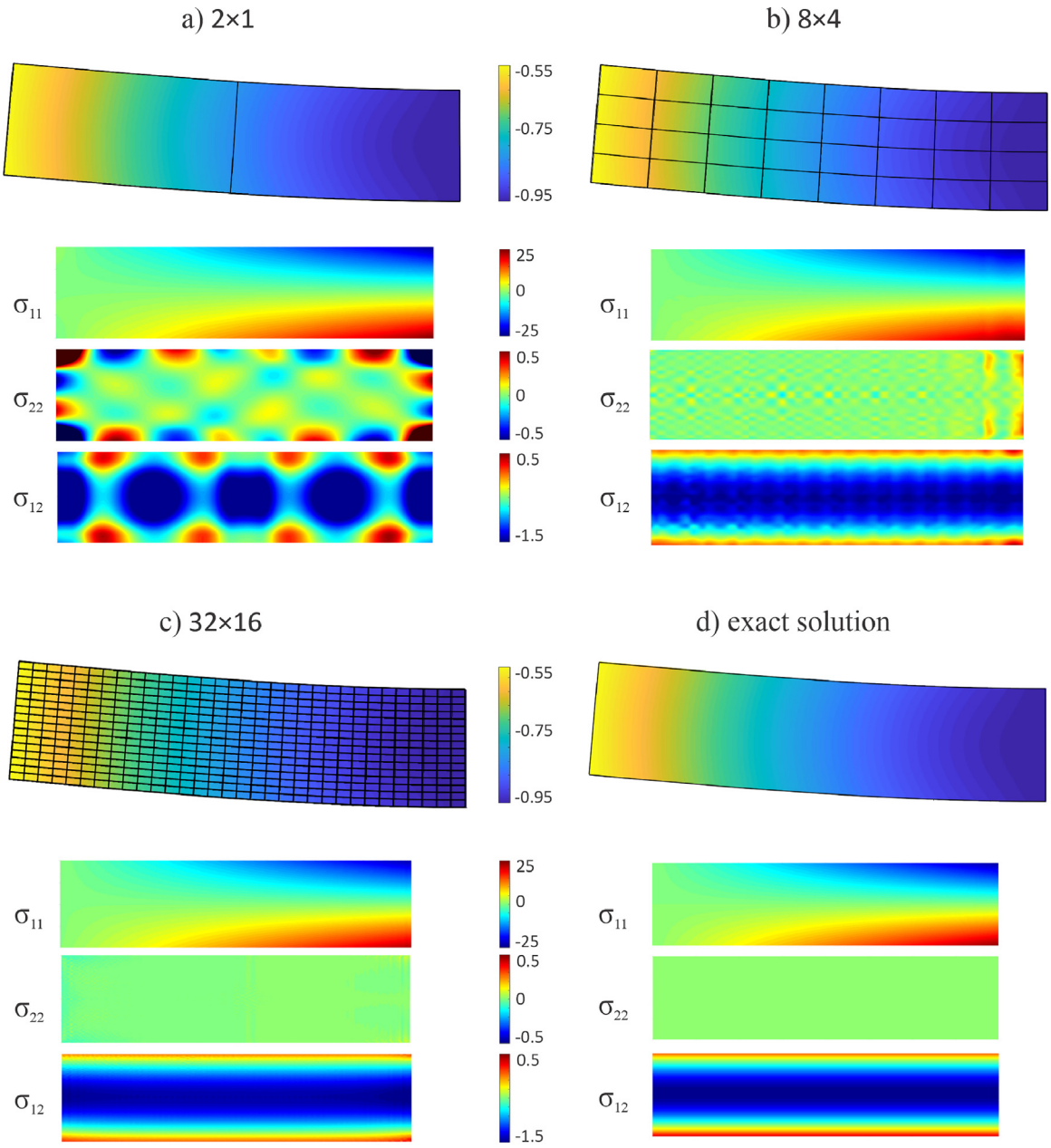

Fig. 14. Mesh refinement shown on the displacements, and corresponding stress contours for the cantilever problem.

The main challenge of the usage of the proposed method is computational efficiency. The hierarchical structure of the blending splines leads to a drastic increase in the number of basis functions with increasing the local degree of the spline surface and requires the accurate computation of the corresponding integrals. Additional research on the algorithm efficiency is required, such as improving the numerical evaluation of integrals related to the blending spline basis functions, which was studied in [32], parallelization of the computational process, etc.

In addition, the tensor product representation is limited in terms of approximation possibilities. An alternative solution to this issue is to develop blending spline basis function spaces defined on the triangle- or polygonal-based meshes.

We believe that the blending spline construction can be successfully applied to real problems, when a combination of strong locality, high spline degree, and smoothness is essential. However, further studies need to be performed to investigate opportunities in a wider variety of problems. We plan to expand possible utilization of the blending spline type constructions by developing new methods and algorithms, in particular, implementation of other element types, adaptive refinement schemes, and automatic mesh generation.

References

[1] T.J.R. Hughes, J.A. Cottrell, Y. Bazilevs, Isogeometric analysis: CAD, finite elements, NURBS, exact geometry and mesh refinement, Comput. Methods Appl. Mech. Engrg. 194 (2005) 4135–4195.
[2] J.A. Cottrell, A. Reali, Y. Bazilevs, T.J.R. Hughes, Isogeometric analysis of structural vibrations, Comput. Methods Appl. Mech. Engrg. 195 (2006) 5257–5296.
[3] W. Li, N. Nguyen-Thanh, K. Zhou, Geometrically nonlinear analysis of thin-shell structures based on an isogeometric-meshfree coupling approach, Comput. Methods Appl. Mech. Engrg. 336 (2018) 111–134.
[4] P. Tan, N. Nguyen-Thanh, T. Rabczuk, K. Zhou, Static, dynamic and buckling analyses of 3D FGM plates and shells via an isogeometric-meshfree coupling approach, Compos. Struct. (ISSN: 0263-8223) 198 (2018) 35–50.
[5] Y. Bazilevs, V.M. Calo, T.J.R. Hughes, Y. Zhang, Isogeometric fluid–structure interaction: theory, algorithms, and computations, Comput. Mech. 43 (2008) 3–37.
[6] H. Gomez, V.M. Calo, Y. Bazilevs, T.J.R. Hughes, Isogeometric analysis of the Cahn-Hilliard phase-field model, Comput. Methods Appl. Mech. Engrg. 197 (2008) 4333–4352.
[7] Y. Bazilevs, L. Beirao de Veiga, J.A. Cottrell, T.J.R. Hughes, G. Sangalli, Isogeometric analysis: approximation, stability and error estimates for *h*-refined meshes, Math. Models Methods Appl. Sci. 16 (2006) 1031–1090.
[8] J.A. Cottrell, T.J.R. Hughes, A. Reali, Studies of refinement and continuity in isogeometric analysis, Comput. Methods Appl. Mech. Engrg. 196 (2007) 4160–4183.
[9] Y. Bazilevs, V.M. Calo, J.A. Cottrell, J. Evans, T.J.R. Hughes, S. Lipton, M.A. Scott, T.W. Sederberg, Isogeometric analysis using T-splines, Comput. Methods Appl. Mech. Engrg. 199 (2010) 229–263.
[10] C. Giannelli, B. Jüttler, S.K. Kleiss, A. Mantzaflaris, B. Simeon, J. Špeh, THB-splines: An effective mathematical technology for adaptive refinement in geometric design and isogeometric analysis, Comput. Methods Appl. Mech. Engrg. 299 (2016) 337–365.
[11] K.A. Johannessen, T. Kvamsdal, T. Dokken, Isogeometric analysis using LR B-splines, Comput. Methods Appl. Mech. Engrg. 269 (2014) 471–514.
[12] K.A. Johannessen, F. Remonato, T. Kvamsdal, On the similarities and differences between classical hierarchical, truncated hierarchical and LR B-splines, 291, 2015, pp. 64–101.
[13] L.T. Dechevsky, A. Lakså, B. Bang, Expo-rational B-splines, Int. J. Pure Appl. Math. 27 (3) (2006) 319–367.
[14] L.T. Dechevsky, P. Zanaty, Smooth GERBS, orthogonal systems and energy minimization, in: Applications of Mathematics in Engineering and Economics 2013, vol. 1570, 2013, pp. 135–162.
[15] L.T. Dechevsky, P. Zanaty, First instances of univariate and tensor-product multivariate generalized expo-rational finite elements, in: Applications of Mathematics and Engineering and Economics 2011, vol. 1410, American Institute of Physics, 2011, pp. 128–138.
[16] P. Zanaty, Finite element methods based on a generalized expo-rational B-splines with harmonic polynomial coefficients, Int. J. Appl. Math. 26 (3) (2013) 379–390.
[17] R. Dalmo, Local refinement of ERBS curves, in: V. Pasheva, G. Venkov (Eds.), 39th International Conference Applications of Mathematics in Engineering and Economics, vol. 1570, AIP Publishing, 2013, pp. 204–211.
[18] R. Dalmo, J. Bratlie, B. Bang, A. Lakså, Smooth spline blending surface approximation over a triangulated irregular network, Int. J. Appl. Math. 27 (1) (2014) 109–119.
[19] L.T. Dechevsky, P. Zanaty, A. Lakså, B. Bang, First instances of generalized expo-rational finite elements on triangulations, in: Applications of Mathematics and Engineering and Economics 2011, vol. 1410, American Institute of Physics, 2011, pp. 49–61.
[20] T. Kravetc, Polygonal blending splines in application to image processing, NIK Norsk Inf. (1) (2021) 113–135.
[21] A. Lakså, Basic Properties of Expo-Rational B-Splines and Practical Use in Computer Aided Design (Ph.D. thesis), University of Oslo, 2007.
[22] T. Kravetc, R. Dalmo, Finite element application of ERBS extraction, J. Comput. Appl. Math. 379 (2020) 112947.
[23] M.G. Larson, F. Bengzon, The Finite Element Method: Theory, Implementation and Practice, Springer, 2010.
[24] T.J.R. Hughes, The finite element method: Linear static and dynamic finite element analysis, Comput.-Aided Civ. Infrastruct. Eng. 4 (3) (1989) 245–246.
[25] O.C. Zienkiewicz, R.L. Taylor, J.Z. Zhu, The Finite Element Method: its Basis and Fundamentals, 6th edition, Elsevier Butterworth-Heinemann Linacre House, Jordan Hill, Oxford, 2005.
[26] G. Strang, G.J. Fix, an Analysis of the Finite Element Method, Prentice-Hall, Englewood Cliffs, NJ, 1973.
[27] O.C. Zienkiewicz, Achievements and some unsolved problems of the finite element method, Internat. J. Numer. Methods Engrg. 47 (2000) 9–28.
[28] X. Feng, H. Wu, Discontinuous Galerkin methods for the Helmholtz equation with large wave number, SIAM J. Numer. Anal. 47 (2009) 2872–2896.
[29] L. Mu, J. Wang, X. Ye, S. Zhao, A numerical study on the weak Galerkin method for the Helmholtz equation with large wave numbers, 2011, arXiv e-prints, arXiv:1111.0671.
[30] J. Koko, Vectorized Matlab codes for linear two-dimensional elasticity, Sci. Program. 15 (2007) 157–172.
[31] S.P. Timoshenko, J.N. Goodier, Theory of Elasticity, McGraw-Hill, New York, 1970.
[32] P. Zanaty, Numerical quadratures for approximate computation of ERBS, in: Applications of Mathematics in Engineering and Economics 2013, vol. 1570, American Institute of Physics, 2013, pp. 180–190.